Supplementary file

Numerical simulation study on power-law acid flow in rough fractures of carbonate rocks

Xu Liu[1,2], Qin Li[1,2,*], Wenling Chen[1,2], Na Li[1,2,*], Yan Huang[3], Huazhou Li[4]

[1] *College of Energy, Chengdu University of Technology, Chengdu 610059, P. R. China*

[2] *State Key Laboratory of Oil and Gas Reservoir Geology and Exploitation, Chengdu University of Technology, Chengdu 610059, P. R.China*

[3] *Zhundong Drilling Company of CNPC Xibu Drilling Engineering Co., Ltd., Urumqi 834000, P. R.China*

[4] *School of Mining and Petroleum Engineering, Faculty of Engineering, University of Alberta, Edmonton T6G 1H9, Canada*

E-mail address: lllxxx1021@163.com (X. Liu); cdutliqin@163.com (Q. Li); cwl851@163.com (W. Chen); lina@mail.ustc.edu.cn (N. Li); wupinren1@163.com (Y. Huang); huazhou@ualberta.ca (H. Li)}.

[*] Corresponding author (ORCID: 0000-0005-0029-3004 (Q. Li); 0000-0002-5787-6332 (N. Li))

Liu, X., Li, Q., Chen, W., Li, N., Huang, Y., Li, H. Numerical simulation of power-law acid flow in rough fractures of carbonate rocks. Advances in Geo-Energy Research, 2025, 17(3): 226-240.

The link to this file is: https://doi.org/10.46690/ager.2025.09.05

Appendix A

(1) Model Assumptions

1) It is assumed that the fluid is in a steady state and incompressible. This means that the flow state of the fluid does not change with time, and the velocity component in the direction perpendicular to the wall surface is negligible. Meanwhile, the density of the fluid remains constant during the flow process.

2) The mass transfer process only has a concentration gradient along the normal direction of the wall surface (the direction perpendicular to the wall surface), and the change in concentration in other directions can be neglected. That is to say, only the diffusion and transfer of the solute in the direction perpendicular to the flat plate are considered, while the concentration is regarded as being uniform in the direction parallel to the flat plate.

(2) The Concept of the Concentration Boundary Layer

When the acid flows over the fracture wall surface, a concentration boundary layer will be formed near the wall surface. Within this region, the concentration of the acid changes from the concentration value at the wall surface to the initial concentration value of the acid (Nasr-El-Din et al., 2009; Peng et al., 2025). The thickness of the concentration boundary layer gradually increases with the increase of the distance from the leading edge of the fracture.

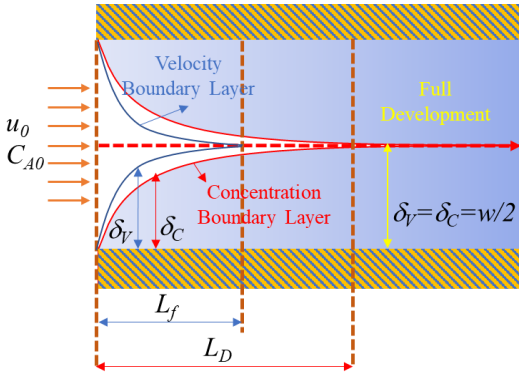

Fig. A1. The formation and development of the boundary layer

(3) Mass Balance of Micro-element Control Volume

Based on the micro-element control volume method (Fig. A2) and the principle of mass conservation, this analysis considers the mass inflow and outflow across each surface of the differential control volume. It is assumed that the length of the differential control volume in the *x*-direction (along the wall) is *dx*, and in the *y*-direction (perpendicular to the wall) is *dy*.

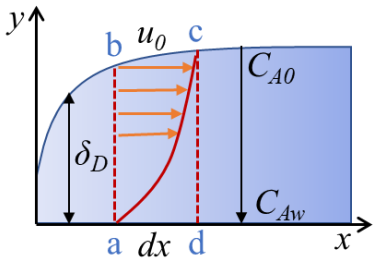

Fig. A2. The diagram of micro-element control volume

In the concentration boundary layer, the amount of substance of H^+ flowing into the *ab* surface of the control volume can be expressed as:

$$M_{ab} = \int_0^{\delta_C} Cudy \qquad \text{(S-1)}$$

where M_{ab} is the amount of substance of H^+ flowing into the ab surface, mol; δ_C is the thickness of the concentration boundary layer, m; C is the H^+ concentration, mol/L; u is the acid flow velocity, m/s.

In the velocity boundary layer, the mass of H^+ flowing into the *ab* surface of the control volume can be expressed as:

$$m_{ab} = \int_0^{\delta_V} \rho udy \qquad \text{(S-2)}$$

where m_{ab} is the mass of H^+ flowing into the ab surface, kg; δ_V is the thickness of the velocity boundary layer, m; ρ is the acid density, kg/m³.

The amount of substance of H^+ flowing into the *bc* surface of the control volume can be expressed as:

$$M_{bc} = \frac{\partial}{\partial x}\left(\int_0^{\delta_C} C_0 udy\right)dx \qquad \text{(S-3)}$$

where M_{bc} is the amount of substance of H^+ flowing into the bc surface, mol; C_0 is the H^+ concentration in the middle of the fracture, mol/L.

The mass of H^+ flowing into the *bc* surface of the control volume can be expressed as:

$$m_{bc} = \frac{\partial}{\partial x}\left(\int_0^{\delta_V} \rho udy\right)dx \qquad \text{(S-4)}$$

where m_{bc} is the mass of H^+ flowing into the bc surface, kg.

The amount of substance of H^+ through the *ad* surface in the control volume can be expressed as:

$$M_{ad} = -D_h \left.\frac{dC}{dy}\right|_{y=0} dx \tag{S-5}$$

where M_{ad} is the amount of substance of H^+ flowing into the bc surface, mol; D_h is the H^+ diffusion coefficient, m^2/s.

The mass of H^+ through the *ad* surface in the control volume can be expressed as:

$$m_{ad} = -D_h \left.\frac{d\rho}{dy}\right|_{y=0} dx \tag{S-6}$$

where m_{ad} is the mass of H^+ flowing into the ad surface, kg.

The amount of substance of H^+ flowing out of the *cd* surface of the control volume can be expressed as:

$$M_{cd} = M_{ab} + \frac{\partial M_{ab}}{\partial x} dx = \int_0^{\delta_C} Cudy + \frac{\partial}{\partial x}\left(\int_0^{\delta_C} Cudy\right) dx \tag{S-7}$$

where M_{cd} is the amount of substance of H^+ flowing into the cd surface, mol.

The mass of H^+ flowing out of the *cd* surface of the control volume can be expressed as:

$$m_{cd} = m_{ab} + \frac{\partial m_{ab}}{\partial x} dx = \int_0^{\delta_V} \rho udy + \frac{\partial}{\partial x}\left(\int_0^{\delta_V} \rho udy\right) dx \tag{S-8}$$

where m_{cd} is the mass of H^+ flowing into the cd surface, kg.

According to the principle of conservation of mass, it is known that:

$$M_{cd} = M_{ab} + M_{bc} + M_{ad} \tag{S-9}$$

$$m_{cd} = m_{ab} + m_{bc} + m_{ad} \tag{S-10}$$

Substituting Eqs. (S-1), (S-3), (S-5) and (S-7) into Eq. (S-9), the integral mass transfer equation of the concentration boundary layer can be obtained:

$$\frac{\partial}{\partial x}\left(\int_0^{\delta_C}\left(C_0 - C\right)udy\right)dx = D_h \left.\frac{\partial C}{\partial y}\right|_{y=0} \tag{S-11}$$

Substituting Eqs. (S-2), (S-4), (S-6) and (S-8) into Eq. (S-10), the integral momentum equation of the velocity boundary layer can be obtained:

$$\rho \frac{d}{dx}\int_0^{\delta_V}\left(u_0 - u\right)udy = \mu \left.\frac{\partial u}{\partial y}\right|_{y=0} \tag{S-12}$$

where u_0 is the acid flow velocity in the middle of the fracture, m/s; μ is the acid dynamic viscosity, Pa·s.

The integral method can be utilized to solve Eqs. (S-11) and (S-12) in order to clarify the expressions of the velocity distribution and the concentration distribution within the boundary layer.

1) Solution of the velocity distribution expression

The velocity distribution in the laminar boundary layer of a flat plate can be obtained through experiments. According to the experimental results, it can generally be expressed in terms of the vertical distance y from the wall surface within the boundary layer:

$$u = a_1 + b_1 y + c_1 y^2 + d_1 y^3 \tag{S-13}$$

The coefficients a_1, b_1, c_1, and d_1 are determined according to the boundary conditions:

① When y=0, since u_x=0, we get a_1 = 0.

② When y=0, since u_x=u_y=0, from the continuity equation, we can obtain $\frac{\partial^2 u}{\partial y^2}=0$, By differentiating Eq. (S-13), we get $\frac{\partial^2 u}{\partial y^2}=2c_1+6d_1 y$. Therefore, c_1=0.

③ When $y=\delta_V$, since $u=u_0$, from Eq. (S-13) with a_1=0 and c_1=0, we get $b_1\delta_V + d_1\delta_V^3=u_0$.

④ When $y=\delta_V$, since $\frac{\partial u}{\partial y}=0$, from Eq. (S-13) with a_1=0 and c_1= 0, we get $b_1 + 3d_1\delta_V^2=0$.

From this, it can be solved that a_1=0, c_1=0, $b_1=3u_0 / 2\delta_V$ and $d_1=-u_0 / 2\delta_V^3$.

Substituting the above coefficients back into Eq. (S-13), the velocity distribution formula of the fluid within the laminar boundary layer can be obtained as follows:

$$\frac{u}{u_0}=\frac{3}{2}\left(\frac{y}{\delta_V}\right)-\frac{1}{2}\left(\frac{y}{\delta_V}\right)^3 \tag{S-14}$$

2) Solution of the concentration distribution expression

Similar to Eq. (S-13), it is assumed that the concentration distribution within the boundary layer can also be expressed in terms of the vertical distance y from the wall surface, that is:

$$C = a_2 + b_2 y + c_2 y^2 + d_2 y^3 \tag{S-15}$$

The undetermined coefficients a_2, b_2, c_2, and d_2 in Eq. (S-15) should satisfy the boundary conditions:

$$\begin{cases} y=0 & C=C_w \\ y=\delta_C & C=C_0 \\ y=\delta_C & \dfrac{\partial C}{\partial y}=0 \\ y=0 & \dfrac{\partial^2 C}{\partial y^2}=0 \end{cases} \tag{S-16}$$

According to the above boundary conditions, the expression of the dimensionless concentration distribution within the boundary layer can be obtained:

$$\frac{C-C_w}{C_0-C_w}=\frac{3}{2}\left(\frac{y}{\delta_C}\right)-\frac{1}{2}\left(\frac{y}{\delta_C}\right)^3 \tag{S-17}$$

where C_w is the H^+ concentration on the fracture surface, mol/L.

3) Solution for the boundary layer thickness

For the derivation of the thickness of the laminar boundary layer, the velocity distribution Eq. (S-14) within the boundary layer can be substituted into the left side of Eq. (S-12) and then integrated:

$$\begin{aligned} &\rho\frac{d}{dx}\int_0^{\delta_V}\left(u_0-u\right)u dy \\ &=\rho u_0^2\frac{d}{dx}\int_0^{\delta_V}\left[1-\frac{3}{2}\left(\frac{y}{\delta_V}\right)+\frac{1}{2}\left(\frac{y}{\delta_V}\right)^3\right]\left[\frac{3}{2}\left(\frac{y}{\delta_V}\right)-\frac{1}{2}\left(\frac{y}{\delta_V}\right)^3\right]dy \\ &=\rho u_0^2\frac{39}{280}\frac{d\delta_V}{dx} \end{aligned} \tag{S-18}$$

Then substitute Eq. (S-14) into the right side of Equation (S-12) and take the derivative:

$$\mu\frac{\partial u}{\partial y}=\mu u_0\frac{\partial}{\partial y}\left[\frac{3}{2}\left(\frac{y}{\delta_V}\right)-\frac{1}{2}\left(\frac{y}{\delta_V}\right)^3\right]\Bigg|_{y=0}=\mu\frac{3u_0}{2\delta_V} \tag{S-19}$$

Substituting the above two equations into Equation (S-12), we get:

$$\rho u_0^2\frac{39}{280}\frac{d\delta_V}{dx}=\mu\frac{3u_0}{2\delta_V} \tag{S-20}$$

By transposing terms and integrating, we obtain:

$$\int_0^{\delta_V}\delta_V d\delta_V=\frac{140\mu}{13\rho u_0}\int_0^x dx \tag{S-21}$$

$$\delta_V = \sqrt{\frac{280}{13}}\left(\frac{\mu x}{\rho u_0}\right)^{1/2} = \sqrt{\frac{280}{13}}x\left(\frac{\mu}{x\rho u_0}\right)^{1/2} = \sqrt{\frac{280}{13}}xRe_x^{-1/2} \quad \text{(S-22)}$$

where v is the kinematic viscosity of the acid, m²/s; Re_x is the Reynolds number of the flow over a length x.

By transposing terms, we get:

$$\frac{\delta_V}{x} = \sqrt{\frac{280}{13}}Re_x^{-1/2} \quad \text{(S-23)}$$

Substitute Eq. (S-14) and Eq. (S-17) into the left side of Eq. (S-11):

$$\frac{d}{dx}\int_0^{\delta_C}(C_0 - C)udy = (C_0 - C_w)u_0\frac{d}{dx}\left[\delta_V\left(\frac{3}{20}(\frac{\delta_C}{\delta_V})^2 - \frac{3}{280}(\frac{\delta_C}{\delta_V})^4\right)\right] \quad \text{(S-24)}$$

Let $\varepsilon = \delta_C / \delta_V$. Assume that the thickness of the flow boundary layer is greater than that of the mass transfer boundary layer, that is $\varepsilon < 1$. So the first term in the brackets is much larger than the second term, and the second term can be neglected. The left side of Eq. (S-11) can be expressed as:

$$\frac{d}{dx}\int_0^{\delta_C}(C_0 - C)udy = \frac{3}{20}(C_0 - C_w)u_0\frac{d(\delta_V\varepsilon^2)}{dx} \quad \text{(S-25)}$$

where ε is the is the ratio of the concentration boundary layer thickness to the velocity boundary layer thickness.

Substituting Eq. (S-17) into the right side of Eq. (S-11), we can obtain:

$$\begin{aligned} D_h\left.\frac{\partial C}{\partial y}\right|_{y=0} &= D_h(C_0 - C_w)\frac{\partial}{\partial y}\left[\frac{3}{2}\left(\frac{y}{\delta_C}\right) - \frac{1}{2}\left(\frac{y}{\delta_C}\right)^3\right]\Bigg|_{y=0} \\ &= D_h\frac{3(C_0 - C_w)}{2\delta_C} \end{aligned} \quad \text{(S-26)}$$

Substituting Eqs. (S-25) and (S-26) into the right side of Eq. (S - 11), we can obtain:

$$\begin{aligned} \frac{3}{20}u_0\frac{d(\delta_V\varepsilon^2)}{dx} &= \frac{3D_h}{2\delta_C} \\ D_h &= \frac{1}{10}u_0\left(\frac{1}{2}\varepsilon^3\frac{d\delta_V^2}{dx} + 2\delta_V^2\varepsilon^2\frac{d\varepsilon}{dx}\right) \end{aligned} \quad \text{(S-27)}$$

Substituting Eq. (S-22) into the right side of Eq. (S-27), we can obtain:

$$D_h = \frac{1}{10}u_0\left(\varepsilon^3\frac{140}{13}+\frac{560}{13}x\varepsilon^2\frac{d\varepsilon}{dx}\right)\frac{\mu}{\rho u_0}$$

$$\varepsilon^3+4x\varepsilon^2\frac{d\varepsilon}{dx}=\frac{13}{14}\frac{D_h\rho}{\mu}=\frac{13}{14}Sc^{-1} \quad \text{（S-28）}$$

$$\varepsilon^3+\frac{4x}{3}\frac{d\varepsilon^3}{dx}=\frac{13}{14}Sc^{-1}$$

The Schmidt number is defined as the ratio of the kinematic viscosity and the diffusion coefficient, so:

$$Sc=\frac{\mu}{\rho D_h}=\frac{v}{D_h} \quad \text{(S-29)}$$

where *Sc* is the Schmidt number.

Integrate Eq. (S-28) by separating variables. If mass transfer starts from $x = x_0$, when $x = x_0$, $\delta_C = 0$, that is $\varepsilon = 0$ at the initial moment; the upper limits are represented by *x* and ε respectively.

$$\int_0^{\varepsilon}\frac{d\varepsilon^3}{\frac{13}{14}Sc^{-1}-\varepsilon^3}=\frac{3}{4}\int_{x_0}^{x}\frac{dx}{x}$$

$$\ln\frac{\frac{13}{14}Sc^{-1}-\varepsilon^3}{\frac{13}{14}Sc^{-1}}=\ln\left(\frac{x}{x_0}\right)^{\frac{-3}{4}} \quad \text{（S-30）}$$

$$\varepsilon=\frac{\delta_C}{\delta_V}=\frac{13}{14\sqrt[3]{Sc}}\sqrt[3]{1-\left(\frac{x}{x_0}\right)^{\frac{-3}{4}}}$$

If H^+ starts mass transfer at the front edge of the fracture and $x_0 = 0$, then:

$$\frac{\delta_C}{\delta_V}=\frac{13}{14\sqrt[3]{Sc}} \quad \text{（S-31）}$$

Substituting Eq. (S-23) into Eq. (S-21), we can obtain the thickness of the mass transfer boundary layer:

$$\delta_C=\frac{13}{14^3\sqrt{Sc}}\times\sqrt{\frac{280}{13}}xRe_x^{-1/2}$$

$$\frac{\delta_C}{x}=\sqrt{\frac{130}{7}}Re_x^{-1/2}Sc^{-1/3} \quad \text{（S-32）}$$

(4) H^+ Mass Transfer Rate

Assuming that the acid concentration on the fracture surface and the main acid concentration in the fluid remain constant, the mass transfer flux of H^+ between the fracture surface and the fluid is given by (Kadafur et al., 2020):

$$N_a = k\left(C_0 - C_w\right) \tag{S-33}$$

where N_a is the mass transfer flux, kmol/(m²·s); k is the mass transfer coefficient, m/s.

The mass transfer flux of H^+ can be expressed based on Fick's law as:

$$N_a = -D_h \left.\frac{dC}{dy}\right|_{y=0} = -D_h \left.\frac{d\left(C - C_w\right)}{dy}\right|_{y=0} \tag{S-34}$$

The simultaneous Eq. (S-33) and Eq. (S-34) obtain:

$$k = D_h \left.\frac{d\left[\left(C_w - C\right)/\left(C_0 - C_w\right)\right]}{dy}\right|_{y=0} \tag{S-35}$$

Substituting Eq. (S-17) into Eq. (S-35), we can obtain:

$$k = \frac{3}{2\delta_C} D_h \tag{S-36}$$

Substituting Eq. (S-32) into Eq. (S-36), and then the local convective mass transfer coefficient k_x at a distance x from the fracture surface can be obtained:

$$k_x = 0.332 \frac{D_h}{x} Re^{1/2} Sc^{1/3} \tag{S-37}$$

where k_x is the local mass transfer coefficient, m/s; x is the vertical distance from the fracture surface, m; Re is the Reynolds number.

The convective mass transfer coefficient in the fracture is:

$$k = \frac{1}{L}\int_0^L k_x dx = 0.664 \frac{D_h}{L} Re^{1/2} Sc^{1/3} \tag{S-38}$$

where L is the characteristic length, specifically the hydraulic diameter of the fluid flow within the fracture.

Since acid fluid systems commonly used in oil and gas fields are generally power-law fluids, for power-law fluids, the apparent viscosity needs to be used to replace the dynamic viscosity of Newtonian fluids. The apparent viscosity is defined as the ratio of the fluid shear stress to the shear rate:

$$\mu_a = \frac{\tau}{\gamma} \tag{S-39}$$

where μ_{app} is the acid apparent viscosity, Pa·s; τ is the shear stress, Pa; γ is the shear rate, s^{-1}.

The shear stress and shear rate of power-law fluids satisfy the following relationship:

$$\tau = K\gamma^n \tag{S-40}$$

where n is the rheological index (dimensionless, $0 < n < 1$).

Therefore, by substituting Eqs. (S-39) and (S-40) into Eq. (S-29), the Schmidt number for power-law fluids can be obtained as follows:

$$Sc = \frac{K}{\rho D_h}\gamma^{n-1} \tag{S-41}$$

Combining Eqs. (1), (2), (S-38) and (S-41), the equation for the H^+ convective mass transfer coefficient in the fracture can be obtained:

$$k = 0.939 w^{\frac{n-2}{2}} u^{\frac{2-n}{2}} \gamma^{\frac{n-1}{3}} \left(\frac{3n+1}{n}\right)^{-\frac{n}{2}} \rho^{\frac{1}{6}} K^{-\frac{1}{6}} D_h^{\frac{2}{3}} \tag{S-42}$$

where w is the fracture width, m; K is the consistency coefficient, $Pa \cdot s^n$.

In high-temperature formations, the surface reaction of H^+ on the fracture surface occurs extremely fast, and the H^+ concentration on the fracture surface is extremely low. Therefore, the H^+ concentration on the fracture surface can be approximated to 0 ($C_w \approx 0$). Then, by combining Eqs. (S-33) and (S-42), the acid-rock reaction rate equation based on mass transfer control can be obtained:

$$J_a = 0.1 N_a = 0.0939 w^{\frac{n-2}{2}} u^{\frac{2-n}{2}} \gamma^{\frac{n-1}{3}} \left(\frac{3n+1}{n}\right)^{-\frac{n}{2}} \rho^{\frac{1}{6}} K^{-\frac{1}{6}} D_h^{\frac{2}{3}} C_0 \tag{S-43}$$

where J_a is the acid-rock reaction rate, $mol/(cm^2 \cdot s)$.

By using the revised formula for the diffusion coefficient in infinitely dilute solutions, the formula for the H^+ diffusion coefficient under different temperatures and acid concentrations was derived as follows (Li et al., 2016):

$$D_h = \left(9.77 \times 10^{-11} e^{0.0847T} C_0 + 1.61 \times 10^{-9} e^{0.023T}\right) / 1000 \mu_a \tag{S-44}$$

where T is the formation temperature, °C.

By combining Eqs. (S-40), (S-41), (S-44) and (S-45), the acid-rock reaction rate equation is:

$$J_a = 0.000939 w^{\frac{n-2}{2}} u^{\frac{2-n}{2}} \gamma^{\frac{1-n}{3}} \left(\frac{3n+1}{n}\right)^{-\frac{n}{2}} \rho^{\frac{1}{6}} K^{-\frac{5}{6}} C_0 \left(9.77\times10^{-11} e^{0.0847T} C_0 + 1.61\times10^{-9} e^{0.023T}\right)^{\frac{2}{3}} \quad \text{(S-45)}$$

Appendix B

To verify the accuracy of the numerical simulation and acid-rock reaction model in this study, acid flow reaction experiments were conducted on cores subjected to Brazilian splitting in this section.

(1) Experimental apparatus

In this study, the acid flow reaction experiment was carried out by using the acidizing conductivity tester (Fig. B1). Its core components include constant current pump, intermediate container, core holder, heating system and data acquisition system.

Fig. B1. Acid flow reaction experimental apparatus

(2) Experimental parameters

The acid utilized in the experiments is gelled acid, whose rheological properties were characterized via rheological testing, yielding a K of 7.8432 and a n of 0.4489. Experimental conditions were maintained at a temperature of 90°C, an acid injection velocity of 0.04 m/s, an injection duration of 5 min, and an initial fracture width of 2 mm, ensuring consistency between experimental and simulation parameters.

(3) Experimental procedures

1) Place the core into the clamping mold, apply red sealant evenly around the core, and carefully place the mold into the core holder. Subsequently, put the core holder into an oven and heat it for 2 hours to ensure the red sealant is fully cured and sealed.

2) Connect the intermediate container, constant-flow pump, and core holder using pipelines. Meanwhile, connect the temperature control device to the core holder, heat the rock plate inside the holder to the formation temperature of 90°C, and maintain this constant temperature for 10 minutes. Then,

open the valve of the intermediate container filled with clean water, start the constant-flow pump, and flush the fracture walls of the rock plate with clean water at a specific flow rate. After flushing, turn off the constant-flow pump and the valve of the clean water-filled intermediate container, open the valve of the intermediate container containing acid and the constant-flow pump, and set the acid flow rate to 0.04 m/s to conduct the acidizing process.

3) After acidizing, turn off the temperature control system and the valve of the acid-filled intermediate container. Reopen the valve of the clean water-filled intermediate container to flush the connected pipelines and the acid-etched fracture walls.

4) Once flushing is completed, turn off the constant-flow pump and all connecting valves. Dismantle the rock plate holder and all connected equipment, carefully take out the core from the holder, and perform cleaning, drying, weighing (note: thoroughly remove the red sealant around the core), and photographing.

5) Use a new-type 3D optical scanner to scan the acid-etched fracture walls, and conduct a series of analysis and processing on the scanning data.

(4) Experimental results

The dissolution mass of the core measured after the experiment was 3.14 g, and the photographs of the core fracture surfaces are shown in Fig. B2. Laser scanning was performed on the fracture surfaces before and after acid etching to obtain the digital models of the fracture surfaces, as shown in Fig. B3.

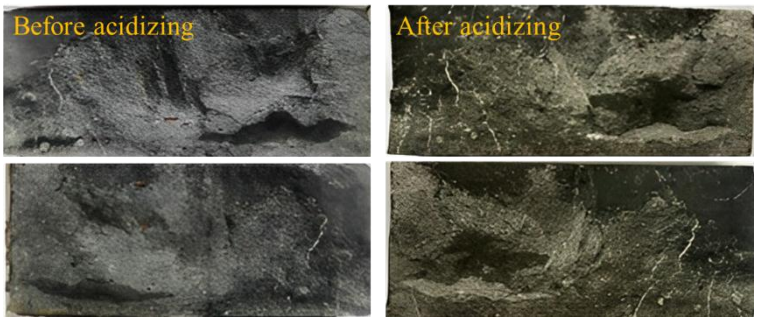

Fig. B2. Photographs of fracture surfaces before and after acidizing

Appendix C

To quantitatively characterize the changes in fracture surface roughness, arithmetic mean height (S_a), root mean square height (S_q), skewness (S_{sk}), kurtosis (S_{ku}), surface development ratio (S_{dr}), and fractal dimension (D) defined in the international standard (ISO 25178) are selected as evaluation parameters in this study, aiming to quantify the complex characteristics of fracture surfaces from multiple dimensions.

These parameters cover the height amplitude, distribution pattern, and spatial structural characteristics of fracture surfaces, enabling comprehensive and accurate characterization of fracture surface roughness.

(1) Arithmetic mean heigh

The arithmetic mean height is defined to reflect the average deviation degree of surface profile heights relative to the midline, and is recognized as a fundamental indicator for characterizing the macroscopic roughness of the surface. Its calculation method is expressed as Eq. (S-46):

$$S_a = \frac{1}{A}\iint_A |z(x,y)|dxdy \tag{S-46}$$

where S_a is the arithmetic mean height; $z(x,y)$ is defined as the height value of any point on the surface profile relative to the reference plane, in *mm*; A is defined as the area of the evaluation region, in mm^2.

As the arithmetic mean height increases, the overall undulation of the surface becomes more pronounced and the roughness degree becomes higher. Good capability in characterizing uniform rough regions on isotropic surfaces is exhibited by arithmetic mean height, and it is suitable for the preliminary evaluation of the average roughness level of fracture surfaces.

(2) Root mean square height

The degree of dispersion of surface heights is reflected by the root mean square height, which is sensitive to extreme peak and valley values. Its calculation method is expressed as Eq. (S-47):

$$S_q = \sqrt{\frac{1}{A}\iint_A z(x,y)^2 dxdy} \tag{S-47}$$

where S_q is the root mean square height. Typically, $S_q \geqslant S_a$; when the height distribution is subject to a normal distribution, $S_q \approx 1.25S_a$.

(3) Skewness

Skewness is used to describe the symmetry of the height distribution of surface profiles and to reflect the relative proportion of convex peaks and concave valleys, with its calculation method given by Eq. (S-48):

$$S_{sk} = \frac{1}{S_q^3 A}\iint_A z(x,y)^3 dxdy \tag{S-48}$$

where S_{sk} is the skewness.

When $S_{sk} = 0$, the height distribution of the fracture surface is symmetric; when $S_{sk} > 0$, the fracture

surface is dominated by convex peaks; when $S_{sk} < 0$, the fracture surface is dominated by concave valleys.

(4) Kurtosis

Kurtosis is used to measure the steepness of the height distribution of surface profiles and to reflect the sharpness or flatness characteristics of peaks and valleys, with its calculation method given by Eq. (S-49):

$$S_{ku} = \frac{1}{S_q^4 A} \iint_A z(x,y)^4 dxdy \tag{S-49}$$

where S_{ku} is the kurtosis.

When $S_{ku} = 3$, the height distribution of the fracture surface is consistent with a normal distribution; when $S_{ku} > 3$, the peaks and valleys of the fracture surface are characterized by sharp features; when $S_{ku} < 3$, the peaks and valleys of the fracture surface are characterized by flat features.

(5) Surface development ratio

The surface development ratio is capable of quantifying the extent of expansion of the actual area of a three-dimensional surface relative to the reference plane, and characterizing the complexity of surface topological structures, with its calculation method given by Eq. (S-50):

$$S_{dr} = \left(\frac{A_{real}}{A_{ideal}} - 1 \right) \times 100\% \tag{S-50}$$

where S_{dr} is the surface development ratio; A_{real} is defined as the actual surface area of the fracture surface, in mm^2; A_{ideal} is defined as the projected area of the reference plane, in mm^2.

When $S_{dr} = 0\%$, the fracture surface is indicated to be an ideally smooth plane; as the surface development ratio increases, features such as surface asperities, pits, and folds are found to be more complex.

(6) Fractal dimension

Fracture surfaces, as typical fractal geometries, exhibit self-similar characteristics in their roughness across multiple scales, and fractal dimension serves as the core parameter for quantifying such cross-scale geometric complexity. The fractal dimension of rough surfaces ranges between 2 and 3; a larger value indicates that details such as surface folds, protrusions, and depressions are more abundant, with fractal characteristics being more prominent.

Currently, various methods for calculating fractal dimension have been developed, among which the box-counting method, spectral dimension method, structure function method, yardstick method, and

carpet covering method are widely applied. The box-counting method does not require estimation of the surface area of rough surfaces during calculation, thus avoiding errors in results. It yields accurate outcomes and can be easily implemented through programming; therefore, the box-counting method is adopted in this study to calculate the fractal dimension of rock fracture surfaces.

In the box-counting method, cubes of the same size are used to cover the rough surface model. By varying the size of the cubes, the number of cubes required to cover the entire fracture surface model under each cube size is obtained. Subsequently, the least squares method is employed to fit the log-log straight line between cube sizes and their corresponding counts, and the slope of this line is the fractal dimension value of the fracture surface morphology.

The proposed three-dimensional rough surface model incorporates an array of δ-sized square grids uniformly distributed across the XY-plane, as schematically depicted in Fig. C1.

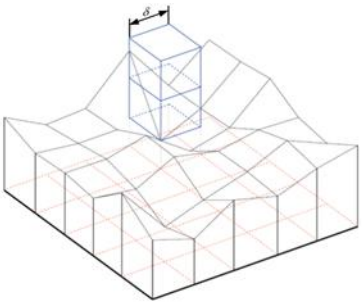

Fig. C1. Schematic diagram of box dimension method

Within each square grid, the four vertices correspond to height coordinates on the curved surface. By tessellating the surface with cubic elements of edge length σ, the minimum number of cubes required to completely cover the three-dimensional surface can be determined through the following expression:

$$\begin{aligned} N_{i,i} = Ceil\{\sigma^{-1}[\max(z(i,j), z(i+1,j), z(i,j+1), z(i+1,j+1)] \\ -\sigma^{-1}[\min(z(i,j), z(i+1,j), z(i,j+1), z(i+1,j+1)]\} \end{aligned} \tag{S-51}$$

where N is the number of boxes; σ is the edge length of boxes, m; "Ceil" represents rounding up to the nearest integer, the number of cubes required is:

$$N(\delta) = \sum_{i,j=1}^{n-1} N_{i,j} \tag{S-52}$$

The size of the cubes is varied, and the corresponding number of cubes required to cover the entire fracture surface model for each cube size is obtained:

$$N(\delta) \propto \delta^{-D} \tag{S-53}$$

where D is the fractal dimension.

The natural logarithm of both sides of the above equation is taken for fitting:

$$\ln N(\delta) \propto D \ln \delta \tag{S-54}$$

Linear fitting is performed on the above data points, and the slope of the resulting straight line corresponds to the fractal dimension D, as shown in Fig. C2:

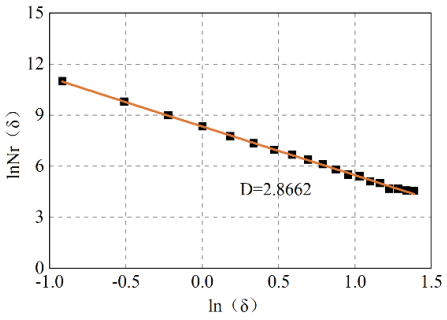

Fig. C2. Fractal dimension fitting value

The specific calculation process is shown in Fig. C3:

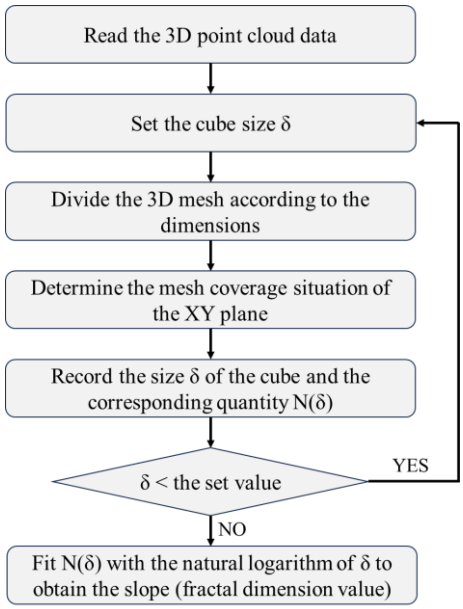

Fig. C3. Flowchart of calculating the fractal dimension by the box dimension method

References

Kadafur, I. B., Aljawad, M. S., Mahmoud, M. Review of acid diffusion measurement methods in porous media. Energy & Fuels, 2020, 34(10): 11916-11941.

Li, Q., Yi, X., Lu, Y., et al. The law of the hydrogen ion diffusion coefficient in acid rock reaction. Journal of Petroleum Science and Engineering, 2016, 146: 694-701.

Nasr-El-Din, H. A., Al-Mohammad, A. M., Al-Aamri, A. D., et al. Quantitative analysis of reaction-rate retardation in surfactant-based acids. SPE Production & Operations, 2009, 24(1): 107-116.

Peng, J., Feng, R., Xue, M., et al. Research progress and engineering applications of viscous fluid mechanics. Applied Sciences, 2025, 15(1): 357.